





Effects of low clay concentrations on nearly isotropic turbulence

Shyuan Cheng ¹, Shaelynn Kaufman,² Vaibhav Tipnis ¹,
James L. Best ^{1,2,3,4} and Leonardo P. Chamorro ^{1,2,4,5,*}

¹*Department of Mechanical Science and Engineering, University of Illinois, Urbana, Illinois 61801, USA*

²*Department of Geology, University of Illinois, Urbana, Illinois 61801, USA*

³*Department of Geography and GIS, University of Illinois, Urbana, Illinois 61801, USA*

⁴*Department of Civil and Environmental Engineering, University of Illinois, Urbana, Illinois 61801, USA*

⁵*Department of Aerospace Engineering, University of Illinois, Urbana, Illinois 61801, USA*



(Received 25 April 2022; accepted 8 July 2022; published 26 July 2022)

We conducted laboratory experiments to quantify the effect of low concentrations of clay, $C \in [0, 2]\%$, on turbulence in water-clay flows under nearly isotropic conditions using a novel approach. Full optical access was possible using Laponite RDTM, a synthetic clay capable of producing clear suspensions of clay particles. Turbulence was generated in a customized cubic mixing box using flow actuators placed symmetrically at each of the eight corners. High-frame-rate particle image velocimetry was used to quantify the spatiotemporal dynamics of turbulence around the center of the mixing box. The results showed that the presence of clay particles strongly modulated the structure of turbulence. Monotonic reduction of the turbulent kinetic energy (TKE) and mean dissipation rate (ϵ) and increase of the Taylor microscale λ was induced by increasing the clay concentration. In particular, the measurements indicated a relation between clay concentration and the p factor, the known Kolmogorov power-law correction $-5/3 + p(\text{Re}_\lambda)$ of the inertial subrange, where Re_λ is the Taylor microscale Reynolds number. The p factor decreased approximately linearly within $1\% \lesssim C \lesssim 2\%$. This parameter and the third-order structure function S_3 supported the scale changes obtained from direct estimation with particle image velocimetry (PIV) data. These results demonstrated the significant impact of clay on the multiscale dynamics of turbulence even at low clay concentrations.

DOI: [10.1103/PhysRevFluids.7.073801](https://doi.org/10.1103/PhysRevFluids.7.073801)

I. INTRODUCTION

Aqueous flows containing various concentrations of clay in suspension are ubiquitous in natural environments and play a pivotal role in landscape formation, riverine and estuarine functioning, ocean geochemistry, and the transport of organic material, pollutants, and nanoparticles. We define transitional water-clay flows as those with a volumetric clay concentration between $0.01 < C < 0.6$ and bounded by clear water and debris flows [1], both of which were studied extensively over the last several decades. These flows containing clay of varying mineralogy and rheological behavior can impart strong modulation on the hydrodynamics, sediment transport, morphodynamic products, and their preserved deposits. As indicated by Baas *et al.* [2], the wall-bounded turbulence of transitional flows may be considerably more complex than the common notion of gradual turbulence damping. Experiments by Amirshahi *et al.* [3] showed distinct modulation of suspended sediments in the dynamics of the near-wall turbulence. In particular, they discussed turbulence enhancement but a reduction of small-scale events. In general, laboratory research has employed primarily acoustic

*Corresponding author: lpchamo@illinois.edu

techniques to characterize turbulence in unidirectional transitional water-clay flows [2] at varying clay concentrations, flow Reynolds numbers, and with kaolinite and bentonite clays [4].

As highlighted by Morris [5], fluid mechanical understanding of suspension, its basic properties, and effects on larger-scale dynamics are central for many processes and applications. Particle interactions in a suspension can significantly modulate the rheological features of the medium [6]. Associated viscosity is controlled substantially by colloidal properties under low shear, including surface charge, particle size distribution, and properties of the suspending medium, such as pH and salinity. However, viscosity is modulated by particle size, shape, arrangement, and distribution under relatively high shear rates [7,8]. Particular efforts focused on investigating the dynamics of drag-reduction in polymer flows and additives [9] and natural clay-laden flows [4,10,11]. Recent experiments demonstrated the presence of a thin layer adjacent to the wall that consists of a low-viscosity fluid, but with the fluid having a significantly higher viscosity outside of this layer [9]. This flow structure is similar to that of shear sheltering in polymer flows at the point of maximum drag reduction [12,13] and that is envisaged for turbulence-enhanced transitional flows in natural clay-laden suspensions [2,4]. Drag-reducing flows possess a thickened viscous sublayer and buffer layer [10], with a significantly larger streamwise Reynolds stress profile but smaller other Reynolds stress components [9], with the exact nature of the stress profiles varying between different types of drag-reducing additive [9]. In addition, some drag-reducing flows reported to possess a larger sublayer spanwise streak spacing than other flows exhibiting high-drag reduction, but this characteristic appears to vary between different types of drag-reducing additive [9]. As such, although much progress has been made on understanding the nature and rheology of flows with additives, we still possess an incomplete knowledge concerning the modification of turbulence in natural clay-laden flows. In particular, our current understanding of the changing dynamics of turbulence across a range of clay concentrations is limited, with the inherent opacity of aqueous clay suspensions limiting detailed quantification to one-dimensional velocity measurements [2].

In the quest for a fundamental understanding of turbulence dynamics across spatial and temporal scales, substantial efforts focused on homogeneous, isotropic turbulence (HIT) since Taylor [14] coined the concept. The statistical properties of HIT, namely invariance to arbitrary translations, rotations, and reflections to the coordinate axes [15], enabled substantial analytical treatment and provided significant insight into various turbulence quantities. A characterization of this type of turbulence has been instrumental in furthering the understanding of both natural and engineered flows. Even though most of these flows are anisotropic, their structure at sufficiently small scales exhibits an isotropic behavior. A vast span of previous research has provided crucial insights into such isotropic turbulence. Kolmogorov [16,17] set one of the most remarkable results in turbulence theory that offers the hallmark for sufficiently high Reynolds number; there is a range of scales between the large nonuniversal and the small that is dominated by viscous dissipation, is locally isotropic, and that exhibits a universal similarity. Wind-tunnel experiments performed with active grids inducing nearly homogeneous, isotropic, turbulence show a modified form of the Kolmogorov similarity law in the inertial subrange that deviates from the well-known $-5/3$ scaling seen at high Taylor-microscale Reynolds number flows [18,19].

Creating homogeneous, isotropic turbulence in the laboratory is challenging, and significant efforts focused on designing experimental setups to achieve this condition. The use of grids in wind or water tunnels has been the most conventional method to induce isotropy, with contractions [20] and active grids [18] proving effective. However, the decaying nature of turbulence in the streamwise direction posed an intrinsic limitation. Significant insights have thus been gained from studies of stationary turbulence with no mean flow in enclosed configurations, which achieved homogeneity and isotropy by stirring the flow with oscillating grids [21]. Opposing oscillating grids in vertical [22] and horizontal [23] arrangements have also been used to minimize the mean flow created by a single grid and compensate for the spatial decay of turbulence away from the grids. However, significant mean flow and anisotropy remain an issue in these setups away from the center plane of symmetry; inhomogeneity of the RMS velocity fluctuations at spatial points aligned with grid nodes versus grid voids in the direction of oscillation poses challenges. Randomly activated jets have also

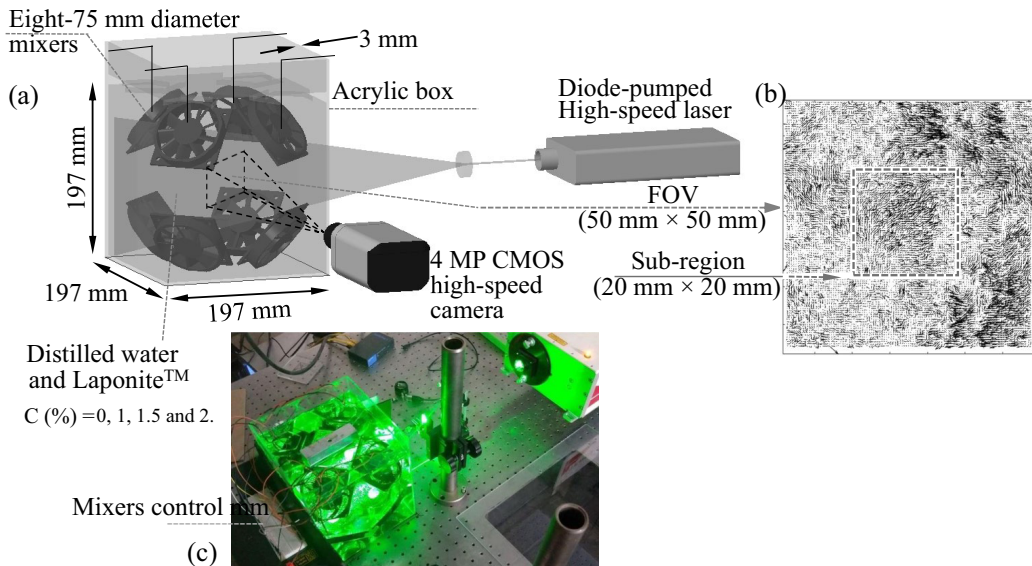


FIG. 1. (a) Basic schematic of the experimental setup, illustrating the mixing box for generating homogeneous and nearly isotropic turbulence, (b) a representative $50 \text{ mm} \times 50 \text{ mm}$ field of view and a $20 \text{ mm} \times 20 \text{ mm}$ subregion located at the center of the box. (c) Photograph of the box and laser illumination.

been used to generate relatively large regions of homogeneous isotropic flow with low variations in turbulence quantities [24,25]. The use of actuators, such as fans, has also been explored over the last few years, with actuators placed at the eight corners of a cube [26,27] or in four corners of a tetrahedron [28] showing promising results. More complex and symmetric setups using a truncated icosahedron geometry have achieved homogeneous and isotropic regions of $\sim 50\text{-mm}$ size and high Taylor microscale Reynolds numbers up to 481 [29,30].

Taking into account design concepts from Birouk *et al.* [26] and Hwang and Eaton [27], we performed flow characterization of transitional clay flows in a homogeneous and nearly isotropic turbulence mixing box with flow actuators placed symmetrically at the eight corners. Here, we illustrate a novel approach to overcome the principal challenges associated with imaging opaque clay flows through the innovative use of Laponite RDTM, a synthetic, smectite clay that behaves in a rheologically similar manner to natural clays [31], but which is capable of producing optically transparent suspensions when dispersed in water at low concentrations. Natural flows containing clays contain both flocs and chains, depending on clay concentration and also the chemistry of the water flow. As such, the presence of these flocs/chains, and their formation and breakup as a function of fluid shear, were reported to be instrumental in turbulence modulation in transitional clay flows using kaolinite and bentonite [2,4]. Consequently, it is reasonable to invoke the formation of such larger particles as also being important in the dynamics of laponite suspensions and their effect on flow turbulence. The study is organized as follows. The experimental setup is described in Sec. II, results and analysis are discussed in Sec. III, with main remarks and implications given in Sec. IV.

II. EXPERIMENTAL SETUP

A. Experimental facility

Experiments were performed in a closed, cube-shaped acrylic box (Fig. 1) constructed of 3-mm-thick acrylic sheets, which housed eight mechanical mixers situated symmetrically in each corner of the cubical chamber and pointing at the box center [26,27]. The inner sides of the box are

197-mm long, and the mixers have a diameter of 75 mm. The chamber has a removable lid at the top to maintain wall boundary conditions on all faces, allow the chamber to be cleaned, and permit insertion of the target plate for particle image velocimetry (PIV) calibration. The dimensions of the box were designed to yield a balance between the quality of turbulence generated and transparency of the Laponite suspensions [32]. Eight Mechatronics Fan Group G8015X12B-AGR-EM thermal management fans were used, each with a dimension of 80 mm × 80 mm × 15 mm and brushless DC actuators with IP-57 water and ingress protection, thereby making them suitable for handling water-clay mixtures without problems of clogging. The fans were connected to a control board powered by a 12-V DC power supply, which allowed fine-tuning of propeller rotation rate. The power cables were routed to the adjustable DC power supply through small holes in the removable lid. Preliminary tests with laponite and kaolinite clays suspensions showed no degradation in performance. During the experiments, a constant rotational speed for each fan was verified using stroboscopic light.

B. Laponite preparation and particle characteristics

The medium consisted of distilled water and Laponite mixtures, which produced fully developed, translucent sols of Laponite RDTM. Distilled water is necessary as the physical properties of the laponite dispersion are highly dependent on the temperature, salinity, and pH of the aqueous solution [33,34]. The white powdered form of Laponite RDTM has a dry state density of $\rho_L = 2530 \text{ kg/m}^3$ and mean diameter $d_L = 30 \text{ }\mu\text{m}$ [35,36]. The powder was dispersed into distilled water using rotational shear in a separate vessel, giving a Stokes particle time constant $\tau_{L,s} = \frac{\rho_L d_L^2}{18\mu} \approx 1.4 \text{ ms}$; where μ is the dynamic viscosity of distilled water. As the powder is spread, hydration and swelling of the clay occur, resulting in a colloidal dispersion that was mixed for a minimum of 20 minutes to ensure complete dispersion and full particle hydration, and yielding a nearly transparent slurry. After reaching complete hydration and exhibiting transparency, the solution was transferred to the mixing box, and mixed continuously to limit large-scale flocculation.

The controlled variable in the experiments is the mass loading fraction of Laponite RDTM defined as $C(\%) = 100 \times M_L/M_f$, which is the ratio between the mass of the dispersed phase laponite $M_L = \rho_L V_L$ and the carrier phase fluid (distilled water) $M_f = \rho_f V_f$ [32]; here $\rho_f = 1000 \text{ kg/m}^3$ is the density of distilled water. The conversion between mass and volume fractions can be obtained by $C_V = (\rho_f/\rho_L)C$, with $\rho_f/\rho_L \approx 0.39$. The present experiments investigated solutions with laponite concentrations of $C = 0\%, 1\%, 1.5\%, \text{ and } 2\%$ with an equivalent $C_V = [0.39 \ 5.8 \ 7.8] \times 10^{-3}$ using the dry state laponite density ρ_L ; note that this is equivalent to a 2.56 times increase in mass loading fraction when considering a hydrated laponite bulk density as this decreases to approximately 1000 kg/m^3 [35,37]. The C_V selected may be considered as dense flow, i.e., $C_V \geq 10^{-3}$ [38,39]. Within this dense flow regime, a momentum transfer exists between particles and flow, which is the so-called two-way coupling [40]. Additionally, particle-particle interactions may also be present and generate a four-way coupling, resulting in a modulated carrier phase turbulence structure [41].

The kinematic viscosity ν of the clear water base case and the various solutions were characterized at standard conditions ($T \approx 25^\circ\text{C}$) after reaching a fully hydrated state, using a Discovery HR-3 Hybrid Rheometer that utilized a standard concentric cylinder geometry. The values given in Table I show a monotonic increase in viscosity with increasing clay concentration. Experimental testing verified no significant aging effect of laponite suspensions at consistently high rates of shear. Testing also confirmed that the clay concentrations were sufficiently low for the solutions to maintain a Newtonian behavior, as shown in Fig. 2.

C. Flow diagnostic system

A nearly transparent laponite solution with refractive index ≈ 1.334 [42] allowed us to utilize high-frame-rate PIV to characterize the turbulence in a 50 mm × 50 mm bulk field of view (FOV) located at the center of the box. The low laponite concentrations did not induce any blurring effects on the clay-water mixtures (see Fig. 3) produced negligible errors in the PIV processing. However,

TABLE I. Basic parameters as a function of clay concentration. An example of a gravel-bed river [59] is included for reference. T_u and T_v : integral timescales of the u and v velocity components; p : scaling factor of the Kolmogorov exponent; Re_λ : Taylor microscale Reynolds number; and $\langle \epsilon \rangle$: mean dissipation rate.

Parameter	$C = 0\%$	$C = 1\%$	$C = 1.5\%$	$C = 2\%$	River flow example [59]
$10^7 \nu$ ($\text{m}^2 \text{s}^{-1}$)	8.9	10.3	11.5	15.1	-
$10^2 \sigma_u$ (m s^{-1})	4.1	3.9	3.5	3.3	3–7
$10^2 \sigma_v$ (m s^{-1})	4.0	3.8	3.6	3.2	2–3
$10^3 q^2$ ($\text{m}^2 \text{s}^{-2}$)	4.7	4.3	3.6	3.1	2–8.7
T_u (s)	0.09	0.15	0.17	0.18	0.59–1.94
T_v (s)	0.10	0.15	0.18	0.21	0.2–0.8
p	0.24	0.23	0.17	0.16	-
n_p	0.26	0.25	0.18	0.17	-
$Re_{\lambda,p}$	102	109	172	257	-
Re_{λ,S_3}	95	106	212	225	-
$10^3 \langle \epsilon \rangle$ ($\text{m}^2 \text{s}^{-3}$)	5.48	4.19	3.26	2.88	-

bias and random PIV errors may occur at sufficiently large concentrations and particle sizes; see Zhang and Rival [43] for details. A 4-MP (2560 pixels \times 1600 pixels) CMOS Phantom M340 camera with 12-GB onboard memory was used to obtain two sets of 2000 image pairs at 100 Hz (see Fig. 1 for details of the experimental setup). The FOV was illuminated with a 1-mm-thick laser sheet generated by a 50-mJ per pulse high-speed, dual cavity Amplitude Nd: YLF laser. The flow was seeded with 55- μm diameter silver-coated, hollow ceramic particles. The image pairs were interrogated using a recursive cross-correlation method in TSI Insight 4G software. The final interrogation window had a size of 32×32 pixels with 50% overlap, resulting in a vector grid spacing $\Delta x = \Delta y = 640 \mu\text{m}$. The PIV setup uncertainty, considering minor camera misalignment and resolution, and laser light sheet alignment, is estimated as 0.2 pixels [44–46], which corresponds to a velocity uncertainty of $\approx 8 \times 10^{-4} \text{m s}^{-1}$. Statistical uncertainty for the velocity variance at each measurement location can be estimated using a chi-square distribution [47] and was negligible for averaging using 2000 image pairs.

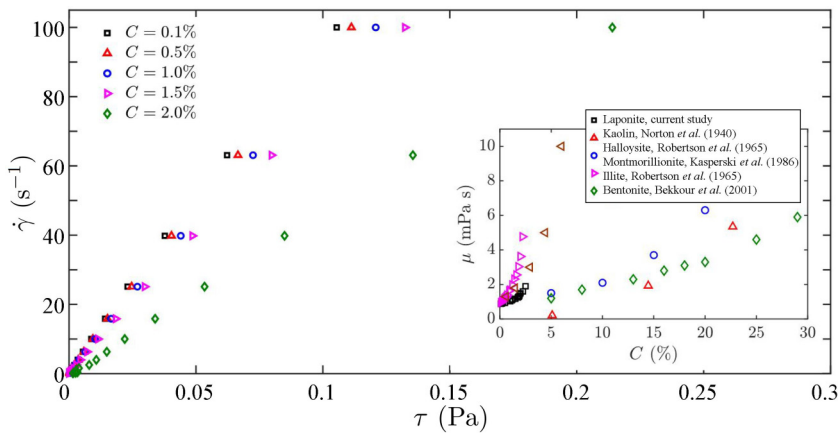


FIG. 2. Shear stress and shear strain rate relationships for strain rates between 0.01s^{-1} to 100s^{-1} at various laponite concentrations C ; inset shows the laponite viscosity μ compared to various types of clays. $\dot{\gamma}$ (s^{-1}).

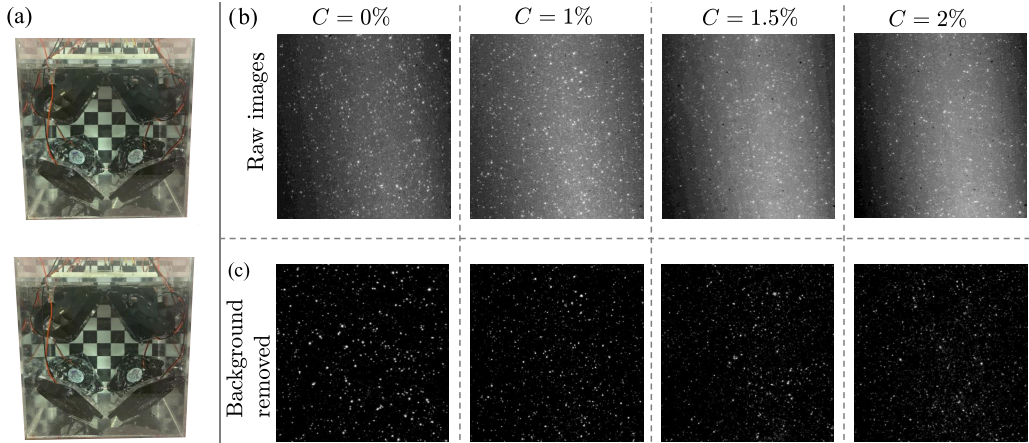


FIG. 3. (a) Photographs of the mixing box with a calibration-type board in $C = 0\%$ (top) and $C = 2.5\%$ (bottom) laponite-water mixtures. (b) Raw PIV image regions of laponite-water mixtures at various concentrations; (c) background-removed images using median subtraction.

D. Unladen clay-free base flow

The clay-free clearwater flow base case was inspected in two perpendicular PIV planes passing through the center of the mixing box. By defining a Cartesian coordinate system located at the center, and denoting u' , v' , and w' as the fluctuating velocity components in the horizontal (u' , v') and vertical (w') directions, we computed the mean velocities (U , V , W) and their associated standard deviations σ_u , σ_v , and σ_w to determine the basic quality of the turbulence. The mean horizontal velocity contour presented negligible mean velocity that was an order of magnitude smaller than the standard deviation of the velocity fluctuations. The isotropy of the base flow is assessed using the spatial variation of the velocity fluctuation ratio, i.e., the so-called isotropic ratios σ_u/σ_v and σ_u/σ_w . The spatial distribution of σ_u/σ_v in Fig. 4(b) shows that this ratio is within $0.95 < \sigma_u/\sigma_v < 1.08$. The probability distribution functions (PDFs) of the u' and v' velocity fluctuations are shown in Fig. 5 and follow a canonical Gaussian distribution well.

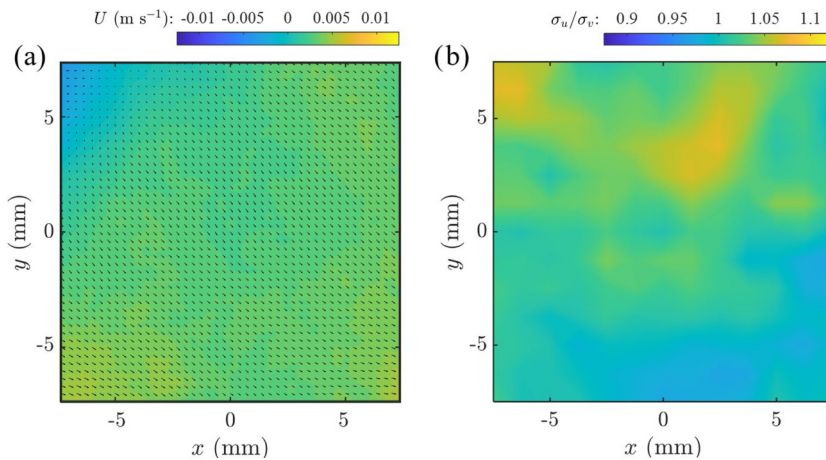


FIG. 4. Distributions of (a) horizontal velocity U and (b) the isotropy ratio σ_u/σ_v for the clay-free base case around the center of the field of view (FOV).

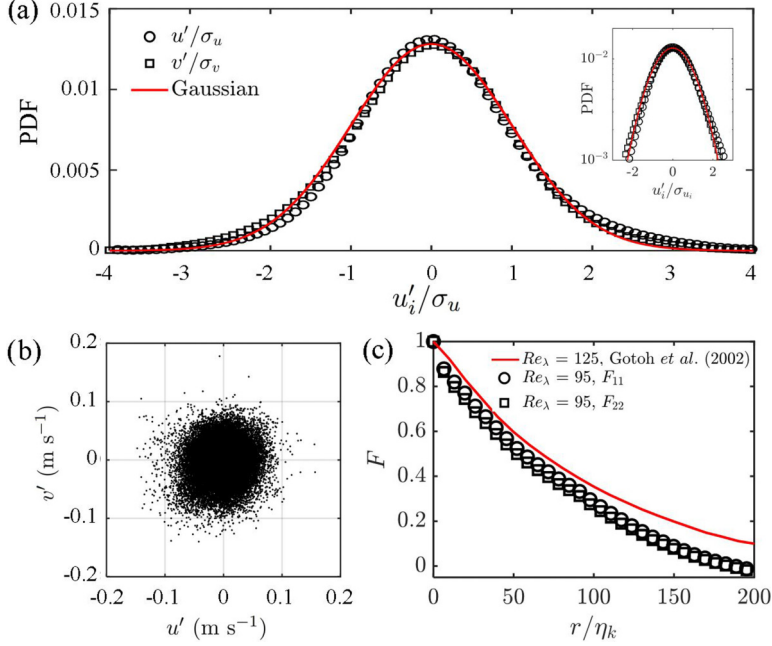


FIG. 5. Quantification of the clay-free flow: (a) PDF of the velocity fluctuations; (b) distribution of velocity fluctuations u' , v' ; and (c) two-point longitudinal velocity correlations for the horizontal, F_{11} , and transverse, F_{22} , directions.

PIV spatial resolution may limit a robust estimation of the Taylor microscale from autocorrelation [48]. Here, the spatial average of the mean dissipation rate $\langle \epsilon \rangle$ is estimated by treating the PIV data as a result of a large eddy simulation approach with a grid resolution of Δx following the procedure proposed by Sheng *et al.* [49], which assumed a dynamic equilibrium at the subgrid scale (SGS) energy flux and approximated the dissipation rate as the energy flux from the SGS scale to the Kolmogorov scale as follows:

$$\epsilon \approx \epsilon_{\text{SGS}} = -2\tau_{\text{SGS},ij}S_{ij}. \quad (1)$$

Here, S_{ij} and $\tau_{\text{SGS},ij}$ are the resolved rate strain tensor and Smagorinsky SGS stress tensor, respectively, with

$$\tau_{\text{SGS},ij} = -C_s^2 \Delta_x^2 |\sqrt{2S_{ij}S_{ij}}| S_{ij}, \quad (2)$$

where $C_s \approx 0.11$ for the 50% overlap and PIV grid resolution [50]. The spatial average of the mean dissipation for the clay-free base case resulted in $5.48 \times 10^{-3} \text{ m}^2 \text{ s}^{-3}$ and has an associated Reynolds number [based on the Taylor microscale of $Re_\lambda = \sigma_u \lambda / \nu \approx 95$; where λ is the Taylor microscale derived from $\lambda = (5\nu q^2 / \langle \epsilon \rangle)^{1/2} \approx 2.03 \text{ mm}$. The Kolmogorov lengthscale corresponding to the dissipation rate is $\eta_k = (\nu^3 / \langle \epsilon \rangle)^{1/4} \approx 9.8 \times 10^{-2} \text{ mm}$. Other estimations of $\langle \epsilon \rangle$ considering $\epsilon \cong 15\nu(\partial_i u'_i)^2$ [51] gives a similar value of $\langle \epsilon \rangle = 5.14 \text{ m}^2 \text{ s}^{-3}$ for $i = 1$ and $\langle \epsilon \rangle = 5.22 \text{ m}^2 \text{ s}^{-3}$ for $i = 2$.

The two-point longitudinal velocity correlation for u' and v' or (u'_1 and u'_2) as a function of the separation distance between the velocity vectors r normalized by η_k is given in Eq. (3) and shown in Fig. 5(c)

$$F_{11}(r) = \frac{\overline{u'_1(x_1, x_2)u'_1(x_1 + r, x_2)}}{u_1'^2}, \quad F_{22}(r) = \frac{\overline{u'_2(x_1, x_2)u'_2(x_1 + r, x_2)}}{u_2'^2}. \quad (3)$$

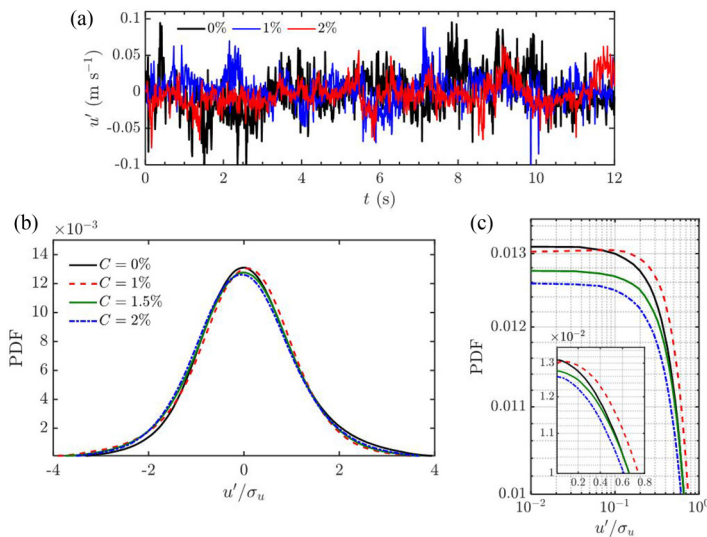


FIG. 6. (a) Sample time series of the horizontal velocity component fluctuations u' for water-clay mixtures at concentrations $C = 0, 1$ and 2% . (b) Probability density functions of the velocity fluctuations. (c) Log-log plot of the velocity fluctuation PDF, with a semi-log-y version in the inset highlighting the distribution for $u'/\sigma_u < 0.8$.

These functions overlap and follow approximately the trend of homogeneous isotropic turbulence data obtained using DNS by Gotoh *et al.* [52] at similar $Re_\lambda = 125$.

III. EFFECT OF CLAY CONCENTRATION

Low concentrations $C \leq 2\%$ of Laponite RDTM produced distinct, measurable changes in the characteristics of the flow. In particular, the turbulence statistics, including the level of velocity fluctuations σ_{u_i} , Reynolds shear stress distribution, and turbulent kinetic energy q^2 exhibited a dependence with C . In addition, the structure of turbulence was sensitive to clay concentration, with the inertial subrange power law of the velocity spectra Φ , the characteristic Taylor microscale λ , and mean energy dissipation $\langle \epsilon \rangle$ also evidencing a modulation with increasing C .

A. Basic flow characteristics

Representative time series of the velocity fluctuations for the base case $C = 0\%$ and flows with clay concentrations of $C = 1\%$ and $C = 2\%$ are illustrated in Fig. 6(a) within the $20 \text{ mm} \times 20 \text{ mm}$ interrogation subregion centered in the FOV [Fig. 1(b)]. These plots illustrate qualitatively the differences in magnitude and nature of intermittent-like fluctuations, revealing the existence of multiscale processes in the clay flows. This may indicate structural differences in the coherent motions induced by various Laponite RDTM concentrations, resulting in modified turbulence dynamics. The probability density functions (PDF) of the normalized velocity fluctuations u'/σ_u for all cases [Fig. 6(b)] show that the lowest clay concentration $C = 1\%$ has a fairly similar distribution to the clay-free base case, whereas minor departures from a Gaussian distribution occurred for $C = 1.5\%$ and $C = 2\%$. These two higher clay concentrations showed a reduced distribution for scales of $u'/\sigma_u \leq 1$ as highlighted in Fig. 6(c). The weakly sub-Gaussian features for $C = 1.5\%$ and $C = 2\%$ suggest the presence of intermittent large-scale events [53], suggesting the occurrence of clay flocs or chains as concentration increases over 1% . It is worth noting that a minor shift to the right in the $C = 1\%$ PDF may be due to secondary flow induced by the clay particles; future investigations around this concentration may offer insights into possible causative mechanisms.

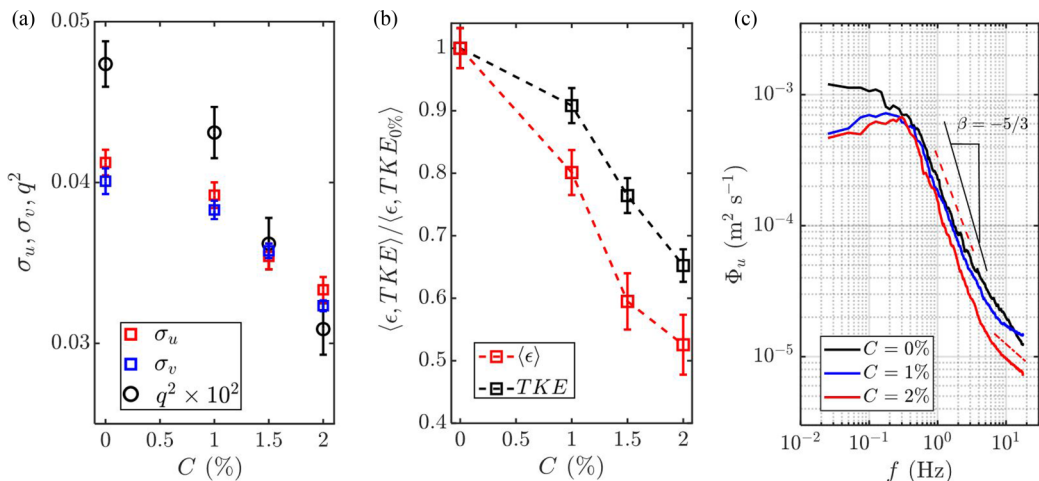


FIG. 7. (a) Variation of second-order statistics σ_u , σ_v and TKE at different laponite clay concentrations. (b) Attenuation of viscous dissipation rate $\langle \epsilon \rangle / \langle \epsilon_{0\%} \rangle$. (c) Velocity spectra for the 20 mm \times 20 mm region of interest at the center of the box.

The second-order statistics obtained with spatial and ensemble averaging for σ_u , σ_v , and turbulence kinetic energy, q^2 , defined as

$$q^2 \equiv \sigma_{u_i} \sigma_{u_i} \cong 3 \frac{\sigma_u^2 + \sigma_v^2}{2} \quad (4)$$

under isotropy, i.e., $\sigma_w \cong \sigma_u$ are illustrated in Fig. 7(a). This reveals a monotonic reduction of the velocity fluctuations and turbulent kinetic energy as clay concentration increases. Figure 7(b) shows the percentage reduction of q^2 and corresponding mean dissipation $\langle \epsilon \rangle$. These measurements also demonstrate an attenuation in mean dissipation as clay concentration increases, with an approximately 50% reduction for the $C = 2\%$ case. Also, $\langle \epsilon \rangle$ decreases at a faster rate compared to q^2 , resulting in the ratio between turbulent kinetic energy (TKE) and dissipation being greater than unity ($q^2 / \langle \epsilon \rangle > 1$), and indicating an increase in Taylor microscale λ as clay concentration increases. It is worth noting the steeper gradient dq^2/dC for $C > 1\%$ compared with $C \leq 1\%$, which results in up to $\approx 35\%$ drop in the value of q^2 from the clay-free base flow. The reduction in q^2 is also apparent from the velocity spectra in Fig. 7(c). Interestingly, the power-law within the inertial subrange deviates from the Kolmogorov $-5/3$ scaling with varying exponents dependent on the clay concentration. An increase in energy in the high-frequency region, $f \gtrsim 10$ Hz [highlighted by the dash-dotted line in Fig. 7(c) for the nonzero clay concentration cases], indicates the existence of small-scale secondary flow structures. An analysis of energy augmentation at the high frequency range, and the dependence between inertial subrange scaling and clay concentration, is given in the following section.

B. On the structure of turbulence

The cross-correlation coefficient, $\overline{u'v'} / (\sigma_u \sigma_v)$, is shown in Fig. 8(a) for the clay-free base case and its corresponding PDF distribution is given in Fig. 8(b) for the $C = 1\%$ and $C = 2\%$ cases. Here, σ_i is the standard deviation of the i component of the velocity. The instantaneous stress distribution for $C = 0\%$ exhibits a nearly zero mean value, indicating the homogeneity and isotropy of the base flow. However, the clay-laden cases exhibit a secondary peak and a slightly positively biased primary peak for the $C = 2\%$ case, which is likely a result of the mean shear caused by secondary flow. The secondary peak increases from 0.12 for $C = 1\%$ to around 0.18 for $C = 2\%$,

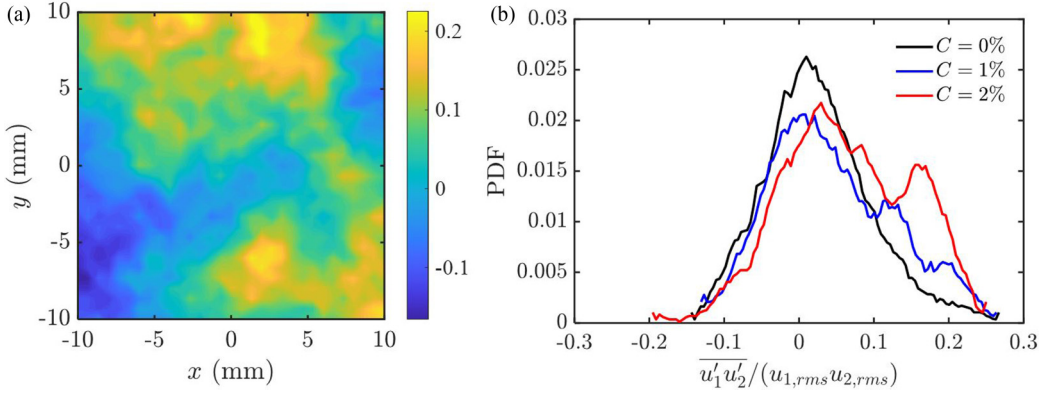


FIG. 8. (a) Contour of shear-stress correlation coefficient for the clay-free base flow. (b) Probability density function of the shear-stress correlation coefficient for the clay-free base flow and two clay concentrations.

indicating the existence of aggregating clay particles that alter the dynamics of energetic structures in the flow responsible for the secondary peak. Note that, despite the secondary peak in shear stress correlation, the flow generally preserves the homogeneous characteristics indicated by the velocity PDF. Additionally, the spatial and temporal velocity correlations shown in Fig. 9 characterize the modification of flow structure by the clay particles. In particular, Fig. 9(a) demonstrates an increase

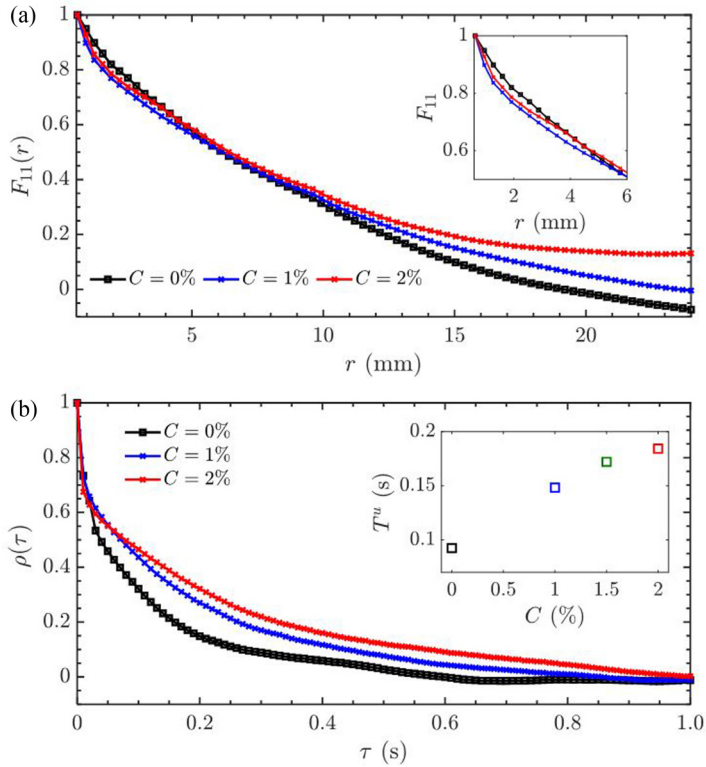


FIG. 9. (a) Correlation of the two-point longitudinal horizontal velocity. (b) Autocorrelation function of the horizontal velocity; inset illustrates the corresponding integral timescale T^u .

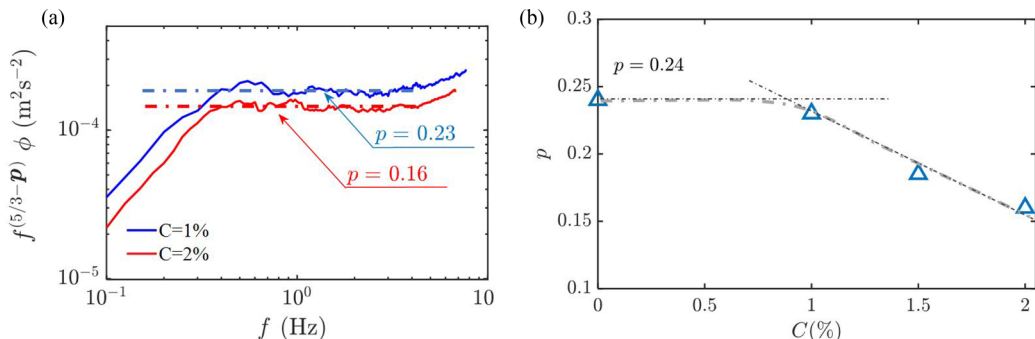


FIG. 10. (a) Compensated velocity spectra, $f^{5/3-p}\Phi$, for the cases with laponite concentrations of $C = 1\%$ (black) and 2% (blue), where the fitted p factors are 0.23 and 0.16, respectively. (b) Power-law correction p as a function of laponite concentration C .

in correlation at the highest clay concentration at large separations (namely, $r \geq 6$ mm) and a decrease at small separations [highlighted in the inset in Fig. 9(a)]. The increase in correlation for $r \geq 6$ mm may indicate that clay flocs/chains transfer energy to the flow via local jet-like fluid motions as they settle [54]. Despite no visual evidence of flocs, the aggregation of clay particles may be present; however, the present experiments did not permit measurement of the possible presence and size of any flocs/aggregates. In contrast, the decrease in correlation with C at small separations may be indicative of small-scale dissipation taking place in the vicinity of the particles, similar to that reported in Tanaka and Eaton [55]. This particular phenomenon deserves further experimental investigation that can aid deriving formulations for numerical models.

Spectral description of the spatial and temporal variability of velocity shows a well-defined inertial subrange with a power scaling $-5/3 + p$, with a correction factor $p \neq 0$ [18] across the cases. By performing a least-squares fit on the compensated temporal spectra $f^{5/3-p}\Phi(f)$ in the flat region defining the inertial subrange, as illustrated in Fig. 10(a) for $C = 1\%$ and 2% , we obtain the dependence of p as a function of clay concentration for the given conditions. The $p - C$ relation for $C(\%) \in [0, 2]$ shown in Fig. 10(b) evidences the change in turbulence dynamics and reveals three features of interest. First, $p = 0.24$ for the case of clear water, which is consistent with the value reported by Mydlarski and Warhaft [18] with $p \approx 0.23$ using their empirical fit at $\text{Re}_\lambda = 95$; second, the onset of changes in p appear in the vicinity of $C \approx 1\%$; third, p exhibits a monotonic decrease with C following an approximately linear trend within $C(\%) \in [1, 2]$, indicating a progression towards the Kolmogorov scaling. This, in turn, implies a change in the associated Reynolds number of the turbulence as examined below.

Mydlarski and Warhaft [18] suggested a correction of the inertial subrange p as a function of the Taylor microscale Reynolds number, given by

$$p = \frac{5}{3}(3.15\text{Re}_\lambda^{-2/3}). \quad (5)$$

This p factor agrees well with that proposed by Puga [19], where the correction factor over the Kolmogorov $-5/3$ scaling as a function of Re_λ is given by

$$n_p = -0.023 + 5.86\text{Re}_\lambda^{-0.645}. \quad (6)$$

The p values from Eqs. (5) and (6) allow for back-calculation of the Taylor microscale Reynolds number of the clearwater case and estimation in the cases with Laponite RDTM (Table I). The calculated Taylor microscale Reynolds numbers range around $100 \lesssim \text{Re}_\lambda \lesssim 260$ in the experimental system, where the only variable changing was clay concentration.

Herein, we also use an alternative approach to examine values of the $p - \text{Re}_\lambda$ relation. In particular, inspection of the third-order structure function $S_3(r) = \langle [u(x+r) - u(x)]^3 \rangle$, where r

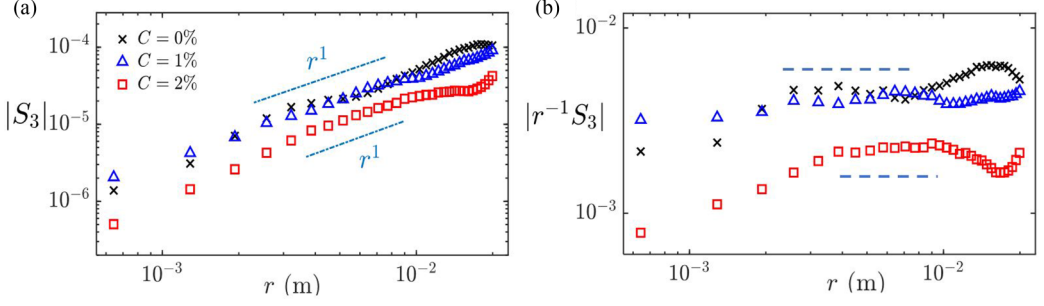


FIG. 11. (a) Third-order structure function S_3 for laponite concentrations of $C = 0\%$ (\times), 1% (Δ), and 2% (\square). (b) Associated compensated counterparts to illustrate the scaling with r .

is the distance and $\langle \rangle$ is the time-averaging operator, allows evaluation and validation of the estimations of Re_λ and energy dissipation. S_3 is related to the mean dissipation $\langle \epsilon \rangle$ by the so-called von Kármán-Howarth-Kolmogorov relation for isotropic turbulence [56] given as

$$S_3(r) = -\frac{4}{5}\langle \epsilon \rangle r + 6\nu \frac{d}{dr} S_2(r), \quad \text{for } \eta_k \ll r \ll L_{11}. \quad (7)$$

At sufficiently high Reynolds numbers, Eq. (7) reduces to $S_3(r) = -\frac{4}{5}\langle \epsilon \rangle r$, allowing direct estimation for $\langle \epsilon \rangle$ [57,58] using a least-squares linear fit of S_3 within the inertial subrange. Although the high Re condition is a stretch for our clay-laden flow, the trend in Fig. 11(b) provides a comparison of the bulk dissipation rate among the various laponite concentrations. The trend is consistent with those $\langle \epsilon \rangle$ estimated from the PIV velocity vector field, with decreasing dissipation at increasing clay concentrations.

The Taylor microscale, $\lambda_{S_3} = [\sigma_u^2 / \langle (\partial_x u)^2 \rangle]^{1/2}$, is also computed using the isotropic relation $\langle \epsilon \rangle = 15\nu \langle (\partial_x u)^2 \rangle$. Selected cases of $S_3(r)$ for $C = 0\%$, 1% , and 2% in Fig. 11 show a shift to higher r in the compensated structure function, $r^{-1}S_3$, for the $C = 2\%$ case [Fig. 11(b)], thus suggesting that an increase in clay concentration may result in a larger Taylor microscale λ . This is consistent with the estimation of $\langle \epsilon \rangle$ obtained with the methods outlined in Sec. II D.

It is worth pointing out that given the spatial resolution of the PIV measurements and the coupling effect from the particles, the formulations provided above are used as estimations for the characteristic scales of the turbulence. These formulations reveal increasing and decreasing trends that provide valuable information that is indicative of the effect caused by water-clay interactions at various clay concentrations. The various turbulence-related quantities discussed for all cases, including the estimated values of the integral timescale T_i for u and v velocity components, correction factor p , associated n_p , the Taylor-microscale-based Reynolds number derived from the p factor $\text{Re}_{\lambda,p}$, the Taylor microscale Reynolds number from the estimation of S_3 (Re_{λ,S_3}), and $\langle \epsilon \rangle$ are summarized in Table I.

C. Characteristic scales

The integral scale L_{11} , Taylor microscale λ , and Kolmogorov lengthscale η_k , are central quantities providing a bulk assessment of turbulence defining the large representative scales and the dissipative motions.

For the range in Laponite RDTM concentration tested ($C \leq 2\%$), an increment in clay concentration leads to larger L_{11} and λ . Although accurate estimation of the integral length scale may be partially limited to our FOV, the increase in L_{11} is likely due to relatively large intermittent-like events, as suggested in Figs. 6(a) and 8(b). In contrast, there is a decrease in $\langle \epsilon \rangle$ modulated by laponite concentration as demonstrated in Figs. 7(b) and 11. This may be counterintuitive in that the typical path for attenuating turbulence is by increasing the dissipation rate, evidencing

a water-clay interaction that alters the turbulence structure within near-isotropic turbulence. An attempt to address the cause of this phenomenon is given in the following section using a basic energy budget analysis [60,61].

D. Energy budget

An energy budget analysis following the procedure of Rogers and Eaton [60] and Hwang and Eaton [54] is carried out here to estimate the additional dissipation as a result of coupling between the particles and turbulence. The energy budget for the fluid-phase kinetic energy, considering steady-state processes for the fluid in the selected control volume, can be written as follows:

$$\dot{E}_{i,f} - \dot{E}_s = 0. \quad (8)$$

Here, $\dot{E}_{i,f}$ is the net energy input rate from the actuator and \dot{E}_s is the energy sink rate. Note that energy output and production rate are not included in the equation since they are negligible in the current system. It is worth elaborating on two major energy sinks in the system. First, the energy rate required to sustain the potential energy of nonbuoyant clay particles, $\dot{E}_{s,p} = CgV_s$, where g is the gravitational acceleration and V_s is the settling velocity obtained from Stokes's equation, i.e., $V_s = \frac{g(\rho_L - \rho_f)d_p^2}{18\mu} = 8.4 \times 10^{-4} \text{ m s}^{-1}$. Second, the viscous dissipation $\dot{E}_{s,v}$ is separated into three parts: (i) the typical turbulent viscous dissipation (ϵ_{sp}) via the turbulent energy cascade, with the dissipation scale bounded by the Taylor microscale λ and Kolmogorov length scale η_k ; (ii) an additional dissipation that occurs near the particle surface with a scale of the particle diameter (ϵ_p ; see Fig. 19 in Tanaka and Eaton [55]) as the result of the additional shear generated between the particle surface and adjacent fluid; and (iii) a dissipation resulting from large-scale flow distortion and particle clustering (ϵ_{ls}) discussed earlier due to four-way coupling. Then, $\dot{E}_{s,v}$ can be separated into ϵ_{sp} , ϵ_p , and ϵ_{ls} , and thus Eq. (8) becomes

$$\dot{E}_{i,f} + CgV_s - \epsilon_{sp} - \epsilon_p - \epsilon_{ls} = 0. \quad (9)$$

A basic estimation of ϵ_p considering quasisteady particle drag by adding a nonlinear correction to the standard Stokes drag is given by Rogers and Eaton [60], Elghobashi and Abou-Arab [62]:

$$\epsilon_p = \frac{\bar{\Phi}}{\rho_f \tau_{L,s}} (\overline{u'_i u'_i} - \overline{u'_i v'_i}) + \frac{1}{\rho_f \tau_{L,s}} (\overline{\Phi' u'_i u'_i} - \overline{\Phi' u'_i v'_i}) + \frac{1}{\rho_f \tau_{L,s}} (\bar{u}_i - \bar{v}_i) \overline{\Phi' u'_i}, \quad (10)$$

where $\bar{(\)}$ and $\langle \rangle'$ denotes the mean and fluctuation of particle velocity v_i , particle concentration $\Phi = m_L/V_f$ (mass of laponite per unit volume), and $\tau_{L,s}$ is the Stokes time constant of laponite particles given in Sec. II B. With a negligible Φ' for $St_k > 1$ [63], and assuming a negligible particle-fluid velocity fluctuation correlation, Eq. (10) can be reduced to

$$\epsilon_p \simeq \frac{\bar{\Phi}}{\rho_f \tau_{L,s}} \overline{u'_i u'_i} = \frac{C \overline{u'_i u'_i}}{\tau_{L,s}}. \quad (11)$$

Using Eq. (9) with the theoretical ϵ_p , we estimate the magnitude of ϵ_{ls} , and take $\dot{E}_{i,f} = \epsilon_{C=0\%} = 5.5 \times 10^{-3} \text{ m s}^{-1}$ as the fan energy input that is dissipated in the clay-free base case to reach equilibrium. All the terms in Eq. (9) are shown in Fig. 12 for all cases and indicate a negligible CgV_s that is an order of magnitude smaller than the other terms. Note that $\dot{E}_{s,p}$ estimation uses the raw laponite particle size; however, a negligible potential energy term would still hold, accounting for the flocculation effect due to a drop in bulk density of laponite to approximately 1000 kg/m^3 [35], resulting in an $V_s \approx 0$ estimation. A low ϵ_{ls} value for $C = 1\%$ shown in the inset to Fig. 12 suggests that the $C = 1\%$ case had much weaker large-scale clustering compared to higher clay concentrations. Note that we use Eq. (11) to obtain a bulk trend estimation of the extra dissipation ϵ_p , but do not rely on the exact quantitative value, as this has been reported to possess errors associated with the quasisteady drag assumption for the flow adjacent to particles [54,64]; other errors also occur due to the current cases not satisfying the $St_k \rightarrow \infty$ assumption. However, this still provides

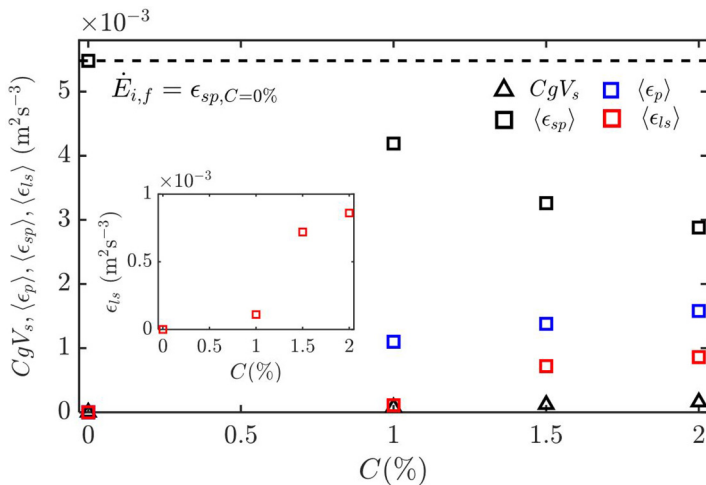


FIG. 12. Terms of Eq. (9) versus clay concentration $C(\%)$; inset shows detailed distribution of $\langle \epsilon_{ls} \rangle$.

an estimation of the order of magnitude of the ϵ_{ls} term, which shows the effect of clay particles on the flow field by modifying the large eddies with a size larger than the Kolmogorov lengthscale η_k . This effect induced by particle addition and clustering likely damped energetic eddies through the so-called “screen effect” proposed by Eaton *et al.* [65] and Hwang and Eaton [54]. This is also suggested by Fig. 9, where the increase in both integral timescale and lengthscale indicate a clustering of particles and that this affects the flow structure.

IV. REMARKS AND CONCLUSION

The experiments reported herein conducted in a specially designed mixing box demonstrate the possibilities and flexibility of using Laponite RDTM to study the poorly understood turbulence-related processes of aqueous transitional clay flows that are ubiquitous in many natural environments. Notable features of laponite suspensions are their optical transparency and a rheology similar to natural clays, enabling characterization and quantification of the effects of clay on turbulence under sufficiently low concentrations with a Newtonian behavior and at a range of shear rates.

Characterization of the statistical quantities of the flow field and flow structure of nearly isotropic turbulence showed the distinct impact of laponite concentration C on the structure of the flow. Notably, the Taylor microscale Reynolds number-dependent scaling correction p of the power law in the inertial subrange, i.e., $-5/3 + p$, exhibited a clear dependence with C , which becomes evident at $C \gtrsim 1\%$ at the shear rate investigated herein, where p decreased approximately linearly with an increase of $C \in (1, 2]\%$. Also, the reduction in the turbulent kinetic energy and mean dissipation rate, and an increase in the Taylor microscale λ , as the clay concentration increases, are shown in estimations using flow field data obtained directly from PIV and the p factor. An energy budget analysis shows that the reduction in turbulent kinetic energy and the increase in λ are likely associated with additional dissipation occurring at a scale larger than the Kolmogorov lengthscale η_k of the clay-free base case, which might result from clay aggregation as shown by the increase in integral time and lengthscales demonstrated for the clay-water mixture.

Our results demonstrate the fundamental importance of these processes, even at low C , and pose many fundamental questions, including the effect of high clay concentrations past the onset of non-Newtonian behavior, the impact of C upon nonisotropic turbulence and the role of changing mean shear rate that is present in natural flows. Subsequent work will focus on particle distribution

measurements and finer spatial resolution to quantify the energy transfer processes across characteristic flow structures within a range of boundary layer flows.

ACKNOWLEDGMENTS

This research was funded by the Campus Research Board Award No. RB20045 at UIUC. The authors appreciate the help of Prof. R. Ewoldt in measuring the viscosity of the clay suspensions.

The authors report no conflict of interest.

-
- [1] R. M. Iverson and C. Ouyang, Entrainment of bed material by earth-surface mass flows: Review and reformulation of depth-integrated theory, *Rev. Geophys.* **53**, 27 (2015).
 - [2] J. H. Baas, J. L. Best, J. Peakall, and M. Wang, A phase diagram for turbulent, transitional, and laminar clay suspension flows, *J. Sediment. Res.* **79**, 162 (2009).
 - [3] S. M. Amirshahi, E. Kwohl, and C. Winter, Near bed suspended sediment flux by single turbulent events, *Continental Shelf Research* **152**, 76 (2018).
 - [4] J. H. Baas, J. L. Best, and J. Peakall, Predicting bedforms and primary current stratification in cohesive mixtures of mud and sand, *Journal of the Geological Society* **173**, 12 (2016).
 - [5] J. F. Morris, Toward a fluid mechanics of suspensions, *Phys. Rev. Fluids* **5**, 110519 (2020).
 - [6] A. Shakeel, H. Mahmood, U. Farooq, Z. Ullah, S. Yasin, T. Iqbal, C. Chassagne, and M. Moniruzzaman, Rheology of pure ionic liquids and their complex fluids: A review, *ACS Sustainable Chem. Eng.* **7**, 13586 (2019).
 - [7] Z. Czibulya, E. Tombácz, T. Szegi, E. Michéli, and Á. Zsolnay, Standard state of soil dispersions for rheological measurements, *Applied Clay Science* **48**, 594 (2010).
 - [8] A. Shakeel, A. Kirichek, and C. Chassagne, Rheology and yielding transitions in mixed kaolinite/bentonite suspensions, *Applied Clay Science* **211**, 106206 (2021).
 - [9] L. Warwaruk and S. Ghaemi, A direct comparison of turbulence in drag-reduced flows of polymers and surfactants, *J. Fluid Mech.* **917**, A7 (2021).
 - [10] G. Gust, Observations on turbulent-drag reduction in a dilute suspension of clay in sea-water, *J. Fluid Mech.* **75**, 29 (1976).
 - [11] G. Gust and E. Walger, The influence of suspended cohesive sediments on boundary-layer structure and erosive activity of turbulent seawater flow, *Marine Geology* **22**, 189 (1976).
 - [12] P. K. Ptasinski, F. T. M. Nieuwstadt, B. Van Den Brule, and M. A. Hulsen, Experiments in turbulent pipe flow with polymer additives at maximum drag reduction, *Flow Turb Combust* **66**, 159 (2001).
 - [13] P. K. Ptasinski, B. J. Boersma, F. T. M. Nieuwstadt, M. A. Hulsen, B. Van den Brule, and J. C. R. Hunt, Turbulent channel flow near maximum drag reduction: simulations, experiments and mechanisms, *J. Fluid Mech.* **490**, 251 (2003).
 - [14] G. I. Taylor, Statistical theory of turbulence-II, *Proc. R. Soc. Lond. A* **151**, 444 (1935).
 - [15] A. S. Monin and A. M. Yaglom, *Statistical Fluid Mechanics, Vols. 1 and 2*, (MIT Press, Cambridge, MA 1975), p. 11.
 - [16] A. N. Kolmogorov, Dissipation of energy in the locally isotropic turbulence, *Dokl Akad Nauk SSSR A* **32**, 16 (1941).
 - [17] A. N. Kolmogorov, The local structure of turbulence in incompressible viscous fluid for very large Reynolds numbers, *C R Acad Sci URSS* **30**, 301 (1941).
 - [18] L. Mydlarski and Z. Warhaft, On the onset of high-reynolds-number grid-generated wind tunnel turbulence, *J. Fluid Mech.* **320**, 331 (1996).
 - [19] A. J. Puga, Characteristics of the velocity power spectrum as a function of Taylor Reynolds number, Ph.D. thesis, UC Irvine, 2016.
 - [20] G. Comte-Bellot and S. Corrsin, The use of a contraction to improve the isotropy of grid-generated turbulence, *J. Fluid Mech.* **25**, 657 (1966).

- [21] I. P. D. De Silva and H. J. S. Fernando, Oscillating grids as a source of nearly isotropic turbulence, *Phys. Fluids* **6**, 2455 (1994).
- [22] S. S. Shy, C. Y. Tang, and S. Y. Fann, A nearly isotropic turbulence generated by a pair of vibrating grids, *Experimental Thermal and Fluid Science* **14**, 251 (1997).
- [23] A. Srdic, H. J. S. Fernando, and L. Montenegro, Generation of nearly isotropic turbulence using two oscillating grids, *Exp. Fluids* **20**, 395 (1996).
- [24] E. A. Variano and E. A. Cowen, A random-jet-stirred turbulence tank, *J. Fluid Mech.* **604**, 1 (2008).
- [25] G. Bellani and E. A. Variano, Homogeneity and isotropy in a laboratory turbulent flow, *Exp Fluids* **55**, 1646 (2014).
- [26] M. Birouk, B. Sarh, and I. Gökalp, An attempt to realize experimental isotropic turbulence at low reynolds number, *Flow, Turbul. Combust.* **70**, 325 (2003).
- [27] W. Hwang and J. K. Eaton, Creating homogeneous and isotropic turbulence without a mean flow, *Exp. Fluids* **36**, 444 (2004).
- [28] D. Bradley, M. Lawes, and M. E. Morsy, Measurement of turbulence characteristics in a large scale fan-stirred spherical vessel, *J. Turbul.* **20**, 195 (2019).
- [29] R. Zimmermann, H. Xu, Y. Gasteuil, M. Bourgoïn, R. Volk, J-F. Pinton, and E. Bodenschatz, The lagrangian exploration module: An apparatus for the study of statistically homogeneous and isotropic turbulence, *Rev. Sci. Instrum.* **81**, 055112 (2010).
- [30] Z. Dou, Z. K. Pecenek, L. Cao, S. H. Woodward, Z. Liang, and H. Meng, PIV measurement of high-Reynolds-number homogeneous and isotropic turbulence in an enclosed flow apparatus with fan agitation, *Meas. Sci. Technol.* **27**, 035305 (2016).
- [31] Y. Lin, H. Qin, J. Guo, and J. Chen, Study on the rheological behavior of a model clay sediment, *JMSE* **9**, 81 (2021).
- [32] J. F. Wallace and C. J. Rutherford, Geotechnical properties of Laponite RDTM, *Geotech. Test. J.* **38**, 574 (2015).
- [33] Y. Zhang, M. Hu, T. Ye, Y. Chen, and Y. Zhou, An experimental study on the rheological properties of Laponite RDTM as a transparent soil, *Geotech Test J* **43**, 20180348 (2020).
- [34] S. Jatav and Y. M. Joshi, Chemical stability of laponite in aqueous media, *Applied Clay Science* **97-98**, 72 (2014).
- [35] K. Suman and Y. M. Joshi, Microstructure and soft glassy dynamics of an aqueous laponite dispersion, *Langmuir* **34**, 13079 (2018).
- [36] B. Zheng, B. Zheng, A. J. Carr, X. Yu, D. J. McClements, and S. R. Bhatia, Emulsions stabilized by inorganic nanoclays and surfactants: Stability, viscosity, and implications for applications, *Inorganica Chimica Acta* **508**, 119566 (2020).
- [37] X-B Huang, J-S Sun, Y. Huang, B-C Yan, X-D Dong, F. Liu, and R. Wang, Laponite: A promising nanomaterial to formulate high-performance water-based drilling fluids, *Pet. Sci.* **18**, 579 (2021).
- [38] S. Elghobashi, On predicting particle-laden turbulent flows, *Appl. Sci. Res.* **52**, 309 (1994).
- [39] S. Elghobashi and G. Truesdell, On the two-way interaction between homogeneous turbulence and dispersed solid particles. i: Turbulence modification, *Phys. Fluids* **5**, 1790 (1993).
- [40] A. Ferrante and S. Elghobashi, On the physical mechanisms of two-way coupling in particle-laden isotropic turbulence, *Phys. Fluids* **15**, 315 (2003).
- [41] M. Alletto and M. Breuer, One-way, two-way and four-way coupled les predictions of a particle-laden turbulent flow at high mass loading downstream of a confined bluff body, *Int. J. Multiphase Flow* **45**, 70 (2012).
- [42] N. R. Kumar, K. Muralidhar, and Y. M. Joshi, On the refractive index of ageing dispersions of laponite, *Applied Clay Science* **42**, 326 (2008).
- [43] K. Zhang and D. E. Rival, Experimental study of turbulence decay in dense suspensions using index-matched hydrogel particles, *Phys. Fluids* **30**, 073301 (2018).
- [44] M. Raffel, C.E. Willert, F. Scarano, C. J. Kähler, S. T. Wereley, and J. Kompenhans, Piv uncertainty and measurement accuracy, in *Particle Image Velocimetry* (Springer, New York, 2018), pp. 203.
- [45] R. J. Adrian and J. Westerweel, *Particle Image Velocimetry*, (Cambridge University Press, Cambridge, England, 2011), p. 30.

- [46] B. Zhang, Y. Jin, S. Cheng, Y. Zheng, and L. P. Chamorro, On the dynamics of a model wind turbine under passive tower oscillations, *Applied Energy* **311**, 118608 (2022).
- [47] J. S. Bendat and A. G. Piersol, *Random Data: Analysis and Measurement Procedures* (John Wiley & Sons, New York, 2011).
- [48] M. Raffel, C. E. Willert, J. Kompenhans *et al.*, *Particle Image Velocimetry: A Practical Guide*, Vol. 2, (Springer, New York, 1998).
- [49] J. Sheng, H. Meng, and R. O. Fox, A large eddy piv method for turbulence dissipation rate estimation, *Chem. Eng. Sci.* **55**, 4423 (2000).
- [50] G. Bertens, D. van der Voort, H. Bocanegra-Evans, and W. van de Water, Large-eddy estimate of the turbulent dissipation rate using piv, *Exp Fluids* **56**, 89 (2015).
- [51] H. Ueda and J. O. Hinze, Fine-structure turbulence in the wall region of a turbulent boundary layer, *J. Fluid Mech.* **67**, 125 (1975).
- [52] T. Gotoh, D. Fukayama, and T. Nakano, Velocity field statistics in homogeneous steady turbulence obtained using a high-resolution direct numerical simulation, *Phys. Fluids* **14**, 1065 (2002).
- [53] J. Jimenez, Turbulent velocity fluctuations need not be Gaussian, *J. Fluid Mech.* **376**, 139 (1998).
- [54] W. Hwang and J. K. Eaton, Homogeneous and isotropic turbulence modulation by small heavy ($st_k \sim 50$) particles, *J. Fluid Mech.* **564**, 361 (2006).
- [55] T. Tanaka and J. K. Eaton, Sub-kolmogorov resolution partial image velocimetry measurements of particle-laden forced turbulence, *J. Fluid Mech.* **643**, 177 (2010).
- [56] A. S. Monin and A. M. Yaglom, *Statistical Fluid Mechanics, Volume II: Mechanics of Turbulence*, Vol. 2, (Courier Corporation, North Chelmsford, MA, 2013).
- [57] M. M. Hoque, M. J. Sathe, J. B. Joshi, and G. M. Evans, Analysis of turbulence energy spectrum by using particle image velocimetry, *Procedia Eng.* **90**, 320 (2014).
- [58] E. O. Akinlabi, M. Waławczyk, J. P. Mellado, and S. P. Malinowski, Estimating turbulence kinetic energy dissipation rates in the numerically simulated stratocumulus cloud-top mixing layer: Evaluation of different methods, *J. Atmos Sci* **76**, 1471 (2019).
- [59] T. Buffin-Bélangier and A. G. Roy, Effects of a pebble cluster on the turbulent structure of a depth-limited flow in a gravel-bed river, *Geomorphology* **25**, 249 (1998).
- [60] C. B. Rogers and J. K. Eaton, The effect of small particles on fluid turbulence in a flat-plate, turbulent boundary layer in air, *Phys. Fluids* **3**, 928 (1991).
- [61] J. R. Fessler and J. K. Eaton, Turbulence modification by particles in a backward-facing step flow, *J. Fluid Mech.* **394**, 97 (1999).
- [62] S. E. Elghobashi and T. W. Abou-Arab, A two-equation turbulence model for two-phase flows, *Phys. Fluids* **26**, 931 (1983).
- [63] K. D. Squires and J. K. Eaton, Particle response and turbulence modification in isotropic turbulence, *Phys. Fluids* **2**, 1191 (1990).
- [64] J. G. M. Kuerten, C. W. M. Van der Geld, and B. J. Geurts, Turbulence modification and heat transfer enhancement by inertial particles in turbulent channel flow, *Phys. Fluids* **23**, 123301 (2011).
- [65] J. Eaton, A. Paris, and T. Burton, Local distortion of turbulence by dispersed particles, in *30th Fluid Dynamics Conference* (American Institute of Aeronautics and Astronautics, Reston, VA, 1999), p. 3643.